Reaction plane correlated triangular flow in Au+Au collisions at $\sqrt{s_{\rm NN}} = 3$ GeV

The STAR Collaboration
(STAR Collaboration)
(Dated: September 13, 2023)

We measure triangular flow relative to the reaction plane at 3 GeV center-of-mass energy in Au+Au collisions at RHIC. A significant v_3 signal is observed for protons, whose magnitude increases for higher rapidity, higher transverse momentum, and more peripheral collisions. The triangular flow is essentially rapidity-odd with a rapidity slope at mid-rapidity, $dv_3/dy|_{(y=0)}$, opposite in sign compared to the slope for directed flow. No significant v_3 signal is observed for charged pions and kaons. Comparisons with models suggest that a mean field potential is required to describe these results, and that the triangular shape of the participant nucleons is the result of stopping and nuclear geometry.

arXiv:2309.12610v1 [nucl-ex] 22 Sep 2023

I. INTRODUCTION

One of the primary goals of the Beam Energy Scan II (BES II), undertaken by the STAR collaboration [1], is to identify and study the transition from hadronic matter to the Quark Gluon Plasma (QGP). At high baryon density, this phase transition is thought to be of first-order [2]. Hence, the understanding of nuclear matter at high baryon density, and its evolution as the phase transition is approached from high to low baryon density, is crucial.

A primary probe of the QGP is the anisotropic flow of particles as they expand outwards which manifests itself in the particle distribution relative to the true reaction plane Ψ_r as a Fourier expansion [3],

$$E\frac{d^3N}{d^3p} = \frac{1}{2\pi}\frac{d^2N}{p_{\rm T}dp_{\rm T}dy}(1+\sum_{n=1}^{\infty}2v_n\cos(n(\phi-\Psi_r))) \quad (1)$$

where $p_{\rm T}, y, \phi$, and Ψ_r are the the particle transverse momentum, rapidity, azimuthal angle, and the true reaction plane angle, respectively. The coefficients in the expansion, v_1 (directed flow), v_2 (elliptic flow), v_3 (triangular flow), etc., describe the collective response of the medium to the shape of the initial collision geometry. They are sensitive to medium properties such as the viscosity and mean-fields that determine the equation of state (EOS).

Anisotropic collective flow has been extensively studied in heavy-ion collisions. Early studies were carried at the Bevelac and at GSI (see [4] for a review) who studied primarily v_1 and v_2 at $\sqrt{s_{NN}} \sim$ a few hundred MeV. Later experiments followed at the AGS ($\sqrt{s_{NN}} \sim 5$ GeV), and the SPS ($\sqrt{s_{NN}} \sim 20$ GeV). A notable feature of collisions at energies $\sqrt{s_{NN}} \lesssim 4$ GeV was the shadowing of outgoing particles by spectators. This lead to phenomena such as squeeze-out leading to in-plane and out-of-plane flow [5]. As research progressed with experiments at RHIC ($\sqrt{s_{NN}} \sim 200$ GeV) and the LHC ($\sqrt{s_{NN}} \sim 5$ TeV), the study of anisotropic flow became increasingly important. The magnitude of v_2, which was best modeled by hydrodynamics, was one of the linchpins in the identification of the Quark-Gluon-Plasma [6]. In addition, the magnitudes of v_2 of mesons and baryons appeared to follow number-of-constituent-quark scaling (NCQ), which provided strong evidence for an expanding partonic medium [7, 8].

The timescale of the collision between the nuclei is a critical element, both in the creation of the medium and in the formation of the initial shape in configuration space. At high energies, above $\sqrt{s_{\rm NN}} = 27$ GeV, where the transit time, $\tau \sim 2R/\gamma\beta$ (where R is the radius of the nucleus, γ is the Lorentz factor, and β is the velocity of the nuclei) is much shorter than the formation time of particles, the spectators are well away from the collision volume and the initial partonic density is free to expand [9]. At these energies, v_3 reflects a hydrodynamic response to event-by-event fluctuations in the initial geometry which is uncorrelated to the reaction plane (i.e. the correlation is with Ψ_3). This v_3 is rapidity even, whose magnitude decreases towards lower $\sqrt{s_{\rm NN}}$. The rapidity-even v_3 has been studied by various experiments, in particular by the STAR collaboration which has reported values of $p_{\rm T}$ integrated v_3 of $\sim 2\%$ at $\sqrt{s_{\rm NN}} = 200$ GeV down to $\sim 1\%$ at 7.7 GeV [10].

This paper reports the observation of v_3 that is *correlated with the reaction plane*[1]. We denote this observable as $v_3\{\Psi_1\}$ (v_3 calculated with the first-order event plane) to distinguish it from the fluctuation-driven v_3 discussed above at higher energies. The measurement of $v_3\{\Psi_1\}$ has also been made by the HADES collaboration in Au+Au collisions at $\sqrt{s_{\rm NN}} = 2.4$ GeV [11, 12]. Our study measures $v_3\{\Psi_1\}$ at comparatively higher energy and introduces comparisons to theoretical models, to gain insight into the origin of the phenomenon.

The development of flow typically hinges on two crucial elements. The first pertains to a geometric shape in spatial configuration space that corresponds to a specific flow coefficient - for instance, an almond shape corresponds to v_2 and a triangular shape corresponds to v_3. This paper discusses a mechanism that produces an initial triangular shape, correlated with the reaction plane resulting from

[1] The term "reaction plane" (as opposed to "event plane") is deliberately used here to describe Ψ_1 as measured in the EPD primarily dominated by spectators in this analysis, as not to confuse it with the usual Ψ_3 which is randomly oriented with respect to the real reaction plane in high energy collisions.

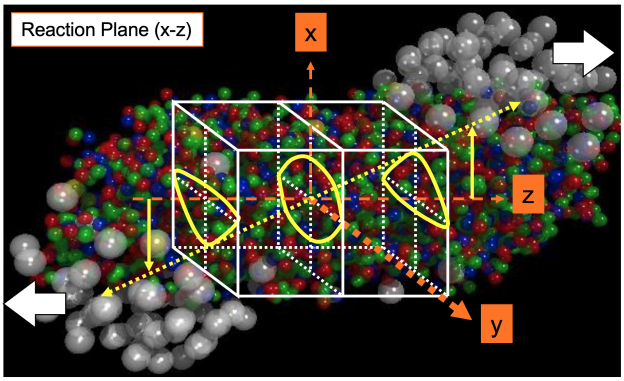

FIG. 1. Cartoon of a non-central heavy-ion collision illustrating the origin of the triangular shape correlated with the event plane (the x-z plane). The forces on the particles resulting from the triangular geometry are perpendicular to the sides of the yellow triangles, opposite to the direction of v_1.

shadowing and baryon stopping. The orientation of this initial triangular shape relative to the reaction plane provides the first necessary element for generating a reaction plane-correlated v_3. Figure 1 presents the geometric illustration[2] of the triangular shape situated in both positive and negative rapidity regions, thereby leading to a flow which is odd in rapidity. We assume positive rapidity is to the right on the plot, hence v_1 is positive [13]. The triangle, for example, shown on the right side of the x-y plane, is oriented with one edge facing in the negative-x direction, aligning in the direction of the pressure gradient and therefore one direction of flow. The other two major directions would be at 60 degrees to the negative-x direction, hence $v_3\{\Psi_1\}$ will be negative at positive rapidity, opposite to that of v_1.

The second element involves the presence of a force which leads to a pressure gradient thereby transforming the spacial configuration to a momentum distribution. At low center-of-mass energies, mean fields provide this force. Flow appears to be sensitive to a variety of parameters that describe these mean fields. Specifically, the incompressibility (K) of matter at high baryon density proves to be of particular importance [14–16]. In the majority of models, mean fields primarily impact baryons, whereas their effects on mesons originate from interactions or decays that involve baryons [17]. Models that integrate a realistic EOS, which includes a transition from a hadron gas to a QGP, will be indispensable for understanding observations in high energy heavy-ion collisions at high baryon density.

[2] While this illustrative model originates from the simulation of higher-energy Au+Au collisions, it is beneficial as it delineates the regions of spectators, participants, and the triangular shape formed by the mechanism outlined in this article.

II. EXPERIMENT

The Solenoidal Tracker at RHIC (STAR) is a multipurpose detector designed to measure hadronic and electromagnetic particles produced in heavy-ion and polarized proton-proton collisions. The STAR comprises several subsystems that provide charged particle tracking and identification over a wide range of pseudorapidity (η) and full azimuth (ϕ) [18]. The primary subsystems used for the present analysis are the Time Projection Chamber (TPC) [19], the barrel Time-of-Flight detector (TOF) [20], and Event Plane Detector (EPD) [21]. The EPD consists of two highly segmented circular detectors positioned at both ends of the TPC and centered around the beam pipe. Each wheel consists of 372 scintillating tiles, enabling a probabilistic determination of the number of Minimum Ionizing Particles (nMIP) passing through each tile per event. The nMIP values are defined within a certainty range of the signal in the scintillator tiles to suppress detector noise and large Landau fluctuations.

In the fixed target (FXT) mode of operation, a single beam strikes a gold foil placed at z = 200.7 cm inside the beam pipe on the west side of STAR, near the edge of the TPC. The target has a thickness of 0.25 mm corresponding to a 1% interaction probability. In this mode, the EPD covers $-5.8 \leq \eta \leq -2.4$ (only the east side can be used), the TPC covers the region $-2 \leq \eta \leq -0.1$, and the TOF covers the range $-1.5 \leq \eta \leq -0.1$ in the laboratory frame; all three subsystems cover the full azimuthal angle.

III. ANALYSIS

A. Event and Track Selection

The Au+Au data set at $\sqrt{s_{\rm NN}} = 3$ GeV was obtained in 2018, with a beam energy of 3.85 GeV per nucleon, in FXT mode. A total of 305M events were available for analysis. Midrapidity ($y_{\rm mid}$) in the laboratory rest frame at this energy is at $y_{\rm mid} = -1.05$, and center-of-mass rapidity is defined as $y_{\rm CM} = y - y_{\rm mid}$. This analysis uses the same sign convention of rapidity as in Ref. [22], where $y_{\rm CM} < 0$ is the forward region and $y_{\rm CM} > 0$ is the backward region; hence the beam direction is towards negative rapidity.

For each event, the reconstructed primary vertex was required to be within 2 cm of the target position along the beam axis. The transverse x, y position of the vertex was required to be within a radius of 1.5 cm from the center of the target. These requirements ensured that the event originated from the gold foil and eliminated beam interactions with the vacuum pipe. The event centrality was estimated from the charged particle multiplicity measured in the TPC and categorized into bins of 5% up to a maximum of 60%. Events with low multiplicity ($<$ 16 primary tracks) or high multiplicity ($>$ 195

primary tracks) were rejected to avoid pile-up. A total of 256M good events remained for further analysis. The remaining pile-up contamination was previously estimated by another STAR analysis at this same energy that studied cumulants of the proton multiplicity distribution. In that analysis, the cumulants were corrected by an unfolding method that statistically separated the single and double collisions in the reconstructed particle multiplicities. This process determined the pile-up fraction to be $(0.46 \pm 0.09)\%$ of all events and $(2.10 \pm 0.40)\%$ in the 0%–5% centrality class [23].

Tracks were required to be reconstructed with at least 15 hit points and greater than 52% of the total possible points to ensure good track fitting quality. Additionally, the Distance of Closest Approach (DCA) to the primary vertex was required to be less than 3 cm to ensure that the tracks originated from the event vertex. Lastly, we required that at least 5 measurements for the average energy loss per unit length ($\langle dE/dx \rangle$) were made for the track.

B. Particle Identification

$\pi^{\pm}$, $K^{\pm}$, and p in this analysis were identified using a combination of $\langle dE/dx \rangle$ measurements from the TPC and mass information calculated from the time-of-flight provided by the TOF. Fig. 2 shows the p_{T} and y_{CM} acceptance of each particle type. Charged pions and kaons are required to have a $\langle dE/dx \rangle$ measurement within 3σ of their expected value, and m^2 measurements within $-0.1 < m^2 < 0.1$ GeV and $0.15 < m^2 < 0.34$ GeV, respectively. Protons do not require a m^2 measurement from the TOF due to their abundance at this collision energy and the fact that, over the relevant momentum range, their $\langle dE/dx \rangle$ curves are well separated from other particles. They are required to have a $\langle dE/dx \rangle$ measurement from the TPC, but we only accept tracks within 2σ of their expected value to reduce the small contamination that may remain at higher momenta. π^+ and π^- used for flow measurements were selected within a range of transverse momentum of $0.18 < p_T < 1.6$ GeV/c, K^+ and K^- within $0.4 < p_T < 1.6$ GeV/c, and p within $0.4 < p_T < 2.0$ GeV/c. Each particle type was selected with a center-of-mass rapidity range of $0 < y_{\mathrm{CM}} < 0.5$. These acceptance regions, which are marked by black boxes in Fig. 2, were used for calculating anisotropic flow vs. centrality. For flow measurements vs. y_{CM}, the acceptance in y_{CM} is extended for protons to $0 < y_{\mathrm{CM}} < 1.0$. Due to the wider range of y_{CM} for protons, we also made a rapidity symmetric acceptance with $-0.5 < y_{\mathrm{CM}} < 0.5$ and $1.0 < p_{\mathrm{T}} < 2.5$ GeV/c (dashed box).

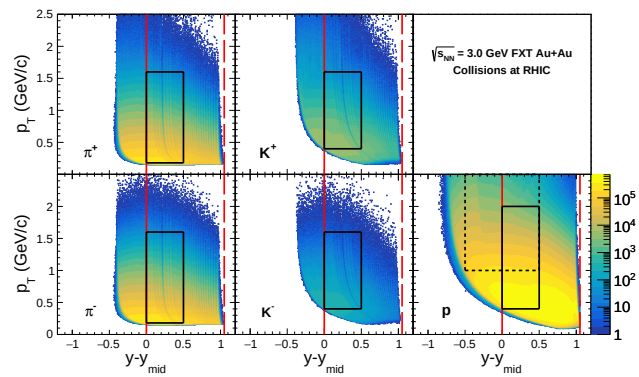

FIG. 2. p_T vs. y_{CM} density plots for $\pi^{\pm}$, $K^{\pm}$, and p measured by the STAR in Au+Au collisions at $\sqrt{s_{\mathrm{NN}}} = 3.0$ GeV. The red dashed line represents the target rapidity and the solid red line represents mid-rapidity. The solid black boxes mark acceptance regions used for flow calculations vs centrality, and the dashed black box marks one of the acceptance regions used for flow vs rapidity.

C. Event Plane Analysis

The event plane method for calculating anisotropic flow was employed in this study. This approach utilizes event plane angles (Ψ_1) reconstructed by a region of the EPD to determine flow coefficients of identified particles in the TPC using

$$v_3 = \langle \cos(3(\phi - \Psi_1)) \rangle / R_{31}, \tag{2}$$

where R_{31} is the resolution correction for the observed reaction plane angle Ψ_1. Here ϕ is the azimuthal angle of an identified particle species, and the averages are taken over all tracks of that particle species and all events of a specific centrality class [3]. For $\pi^{\pm}$ and $K^{\pm}$, the averages are weighted by the inverse of the product of TPC and TOF matching efficiencies. The averages for protons were weighted by only the inverse of the TPC tracking efficiency. To prevent systematic overestimation of flow we applied the resolution correction track-by-track within the average as suggested in Ref. [24].

The event plane resolution R_{31} is calculated for each centrality interval using the standard three-subevent method [3]:

$$R_{31} = \sqrt{\frac{\langle \cos(3(\Psi_1^A - \Psi_1^B)) \rangle \langle \cos(3(\Psi_1^A - \Psi_1^C)) \rangle}{\langle \cos(3(\Psi_1^B - \Psi_1^C)) \rangle}}, \tag{3}$$

where the reaction plane angles Ψ_1^A, Ψ_1^B, and Ψ_1^C are obtained in three η ranges: $-5.8 < \eta_A < -3.2$, $-3.2 < \eta_B < -2.5$, and $-1 < \eta_C < 0$. Equation 3 provides the resolution for subevent A which was used for reconstructing Ψ_1. Regions B and C were only employed for calculating R_{31}, so while the identified particles overlap with region C, there is no auto-correlation effect in the flow measurements.

The weights within the $\vec{Q}$ vectors [3] used for reconstructing event plane angles were p_T in the TPC region and the nMIP values from the EPD with a minimum threshold of 0.3 and maximum of 2.0. In addition, all weights for tracks or hits with $\eta < -1.045$ have a negative sign while all with $\eta > -1.045$ are positive to account for the the fact that v_1 is odd in rapidity. Each event used in the analysis was required to have a minimum of 5 hits in the inner EPD region, 9 hits in the outer EPD region, and 5 tracks in the TPC region to ensure that each subevent had an adequate number of particles to reconstruct Ψ_1.

Before calculating R_{31} and flow, we perform recentering followed by Fourier shifting corrections on all event plane distributions to remove biases from non-uniform detector acceptance [3]. After these corrections, all event plane distributions are isotropic from $-\pi$ to π. The values calculated for the event plane resolution in each centrality are shown in Fig. 3 [25]. These specific values were calculated considering systematic effects and are described in the next section.

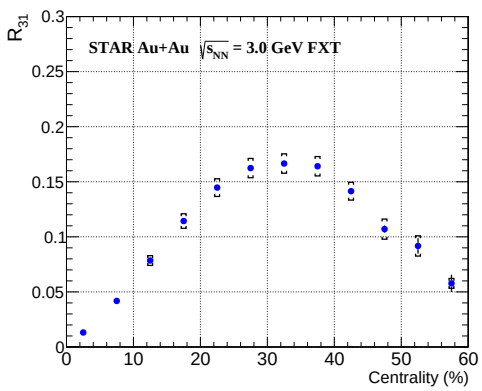

FIG. 3. Event plane resolution for $v_3\{\Psi_1\}$ as a function of centrality from $\sqrt{s_{\rm NN}} = 3$ GeV Au+Au collisions at STAR. The points are the average of the resolutions from the three configurations discussed in Section III D, and the systematic uncertainties are the maximum difference between the configurations and the average (taken as a symmetric uncertainty in the opposite direction as well). Vertical lines are statistical uncertainties and open brackets are systematic uncertainties.

D. Systematic Uncertainties

We varied all track quality and particle identification cuts by 20%, and again by 30%, to estimate the systematic uncertainties contributed by each cut and denoted these as $\sigma_{{\rm sys},i}$, where i would be any of the cuts mentioned in Sections III A and III B. The $\sigma_{{\rm sys},i}$ was calculated as the standard deviation from all 5 measurements of $v_3\{\Psi_1\}$. The final systematic uncertainty for any one $v_3\{\Psi_1\}$ value would then be $\sqrt{\sum_i \sigma^2_{{\rm sys},i}}$, where a check was done and only the cuts with variations deemed significant for that measurement would be included in the sum [26]. The only variation that did not go through this check was for the event plane resolution, which was included for every $v_3\{\Psi_1\}$ measurement.

The maximum values of the resolution, R_{31}, were obtained by utilizing all three subevents described in Section III C. To estimate systematic errors, two variations were implemented to modify the size of region B in the EPD to introduce an η gap between regions A and B. This was done to eliminate potential momentum conservation effects and assess other systematic factors involved in the calculation of R_{31}. One variation involved changing region B to rings 10-16 in the EPD ($-3.1 < \eta < -2.5$), while the other variation replaced it with rings 13-16 ($-2.8 < \eta < -2.5$). By employing the two variations for the event plane from region B, in addition to the initial configuration, an envelope of R_{31} values was established. The average value $\langle R_{31}\rangle$ from all three configurations was adopted as the resolution, and the maximum deviation from this average among the three variations was taken as the systematic error for R_{31} (see Fig. 3). To propagate the uncertainties in R_{31} to variations in flow, the resolutions are increased/decreased by the total uncertainty (statistical plus systematic in quadrature) and flow is calculated.

Table I shows the contribution of each systematic source as a percentage of $v_3\{\Psi_1\}$, averaged across all measurements, in three wide centrality regions. All contributions related to track quality cuts were combined in quadrature and listed in the first row; and the same was done for event selection cuts shown in the second row. The proton $\langle dE/dx\rangle$ contribution in 0-10% centrality is 54% simply due to the very small magnitude of the proton $v_3\{\Psi_1\}$ in this centrality range.

TABLE I. Average contribution of each varied cut to systematic uncertainties in $v_3\{\Psi_1\}$ as a percentage of the $v_3\{\Psi_1\}$ value for three centrality ranges.

Systematic Source	**Uncertainties in Percent**		
Centrality Interval	0-10%	10-40%	40-60%
Track Quality	11.5	4.3	2.5
Event Quality	2.8	0.4	0.5
π $\langle dE/dx\rangle$	4.3	2.8	3.4
K $\langle dE/dx\rangle$	8.9	13.6	0.4
Proton $\langle dE/dx\rangle$	54.3	3.0	6.7
TOF m^2_π	3.2	1.0	1.6
TOF m^2_K	13.3	15.4	1.2
Event Plane Resolution	13.4	5.4	9.0

IV. RESULTS

The $v_3\{\Psi_1\}$ values for $\pi^{\pm}$, $K^{\pm}$, and protons were calculated as a function of centrality and these results are presented in Figs. 4 and 5. Figure 4 specifically shows that, while the values for pions are only slightly negative, the protons exhibit a significant negative $v_3\{\Psi_1\}$ signal that increases with centrality. Figure 5 suggests that $v_3\{\Psi_1\}$ for K^+ may also be consistent with zero, while the available statistics for K^- do not allow for a definitive conclusion. To test the significance of the K^- signal we performed a fit using a constant value at zero. This produced $\chi^2/\mathrm{NDF} = 8.85/5 = 1.77$, hence we can not rule out the possibility that this signal is consistent with zero.

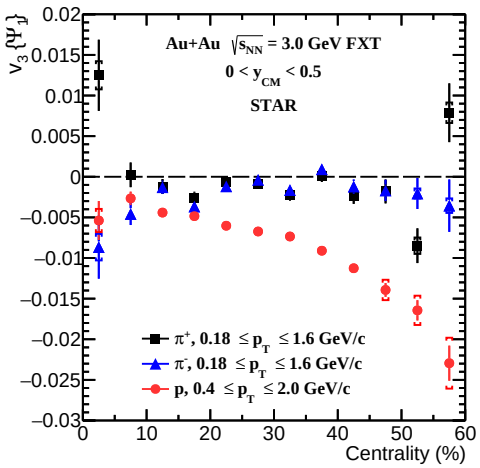

FIG. 4. $v_3\{\Psi_1\}$ vs. centrality for π^+, π^-, and protons using the event plane method. Protons show a clear negative $v_3\{\Psi_1\}$ while pions remain near zero. Statistical uncertainties are shown as lines while systematic uncertainties are denoted by open square brackets.

Fig. 6 displays $v_3\{\Psi_1\}$ values as a function of rapidity in a symmetric acceptance region indicated by the dashed black box in Fig. 2 where the p_T is required to be above 1.0 GeV/c in order to have an acceptance below mid-rapidity. Here we see that the $v_3\{\Psi_1\}$ signal is essentially rapidity-odd. We measure the reaction plane in only the EPD on the negative rapidity side of the collision, hence there may be effects, such as event plane rapidity decorrelations, and $v_3\{\Psi_1\}$ may not strictly speaking be rapidity-odd. However we will speak of $v_3\{\Psi_1\}$ as rapidity-odd since the signal's source is not primarily fluctuations that are even in rapidity as is the case at higher energies. The signal has a clear negative slope around midrapidity. Previous STAR results at this energy [13, 27] show a positive $(dv_1/dy)_{y=0}$ slope; hence, this result demonstrates that the protons' $v_3\{\Psi_1\}|_{y=0}$ has a slope with opposite sign to $(dv_1/dy)_{y=0}$.

In Fig. 7, we additionally present $v_3\{\Psi_1\}$ as a function of rapidity in the backward region $0 < y_{\mathrm{CM}} < 1$, extending the p_T range down to 0.4 GeV/c and we have

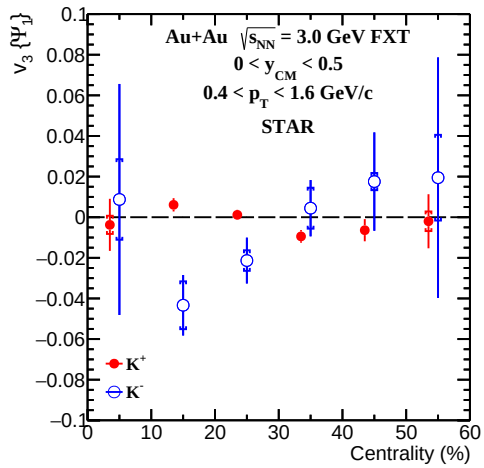

FIG. 5. $v_3\{\Psi_1\}$ vs. centrality for K^+ and K^- using the event plane method. The values for K^+ are slightly shifted horizontally for visual clarity. More statistics are required to fully understand if this signal is present for kaons. Statistical uncertainties are shown as lines while systematic uncertainties are shown as open square brackets.

mirrored the measured points and represented them as open circles. By fitting the function $y = ax + bx^3$, where y is $v_3\{\Psi_1\}$, x is $y - y_{\mathrm{mid}}$, and a is $dv_3/dy|_{y=0}$, to the 10-40% centrality data using only the measured points, we obtain a slope of $dv_3/dy|_{y=0} = -0.025 \pm 0.001$ (stat).

To estimate the systematic error on the slope, we assume that the percentage difference between slope measurements for the positive and negative rapidity sides of Fig. 6 would be similar to the percentage difference for the positive and negative sides (if measurable) of Fig. 7. We utilize both sides of Fig. 6 to calculate $\Delta a/(\langle a\rangle\sqrt{12}) = 0.13$. The systematic error for the slope in Fig. 7 is then determined as $|-0.025| \times 0.13 \sim 0.003$. Therefore, the final measurement of the slope is $dv_3/dy|_{y=0} = -0.025 \pm 0.001$ (stat) ± 0.003 (sys).

In Fig. 8 we present $v_3\{\Psi_1\}$ values from protons vs. p_{T}, showing that the magnitude increases with increasing p_{T}.

Figures 6 - 8 show that the proton $v_3\{\Psi_1\}$ values become increasingly negative towards more peripheral collisions consistent with Fig. 2 with the effect being strongest at the largest p_{T} and rapidity.

V. DISCUSSION

This section will first compare models to data. Subsequently, we provide a more comprehensive discussion of the models, specifically focusing on how the initial geometry and potentials are manifest with particular emphasis on protons. Lastly, a brief discussion of pions and kaons and a comparison to the previous HADES result will follow.

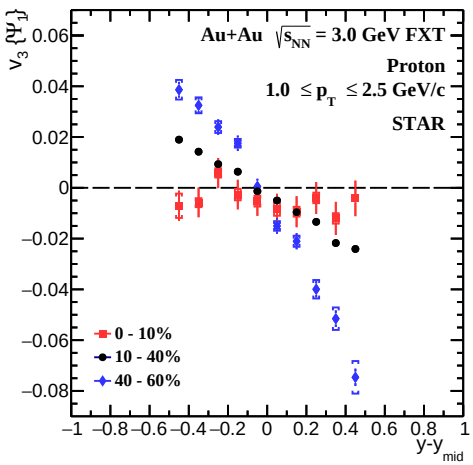

FIG. 6. $v_3\{\Psi_1\}$ vs. rapidity for protons in three large centrality bins from a symmetric acceptance across midrapidity. Protons exhibit an increasingly negative slope going towards more peripheral collisions. Statistical uncertainties are shown as lines while systematic uncertainties are denoted by open square brackets.

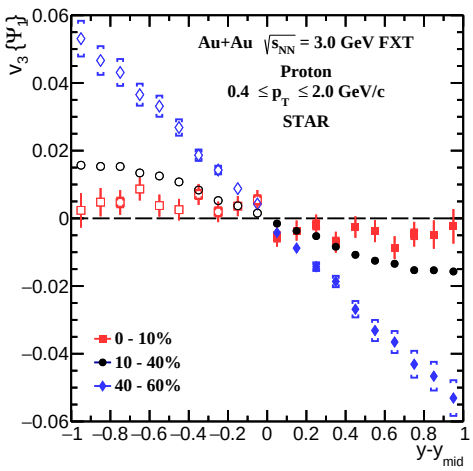

FIG. 7. $v_3\{\Psi_1\}$ vs. rapidity for protons in three large centrality bins from only the backward region (solid markers) along with mirrored points across midrapidity (open markers). Note that the p_T acceptance extended to a lower limit than in Fig. 6. Statistical uncertainties are represented as lines while systematic uncertainties are denoted by open square brackets.

A. Model Comparisons

The results have been compared with several models: AMPT, RQMD, SMASH and JAM [14–16, 28]. For the sake of illustration, we will focus on the JAM and SMASH models.

Each model includes a cascade mode which treats baryons and mesons as individual particles modeling their interactions as if they were colliding billiard balls. The radius of each particle is determined by the cross section and secondary particles are formed according to

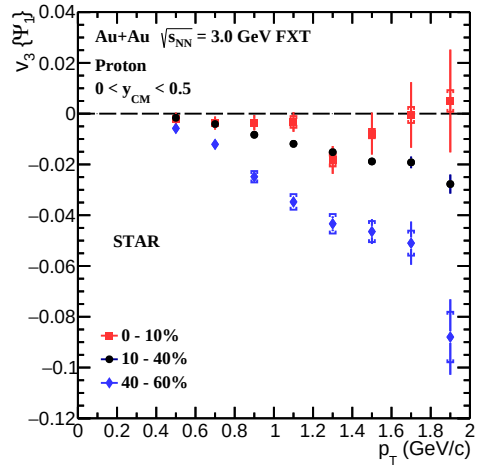

FIG. 8. $v_3\{\Psi_1\}$ vs. p_T for protons in three large centrality bins. $v_3\{\Psi_1\}$ becomes increasingly negative as p_T and centrality increase. Statistical uncertainties are shown as lines while systematic uncertainties are denoted by open square brackets.

known reactions. There is no long range interaction.

At high center-of-mass energy, above $\sqrt{s_{NN}} \sim 30$ GeV, the timescale of the collision is very short relative to the formation time (typically about 1 fm/c) and geometric effects are essentially two-dimensional in the x-y plane. However, at lower energies, the passing time of the two nuclei in a Au+Au collision is long compared to the formation time; at $\sqrt{s_{NN}} = 3$ GeV it is ~ 10 fm/c. This is the energy regime in which baryon stopping becomes dominant[29]. Such a scenario leads to effects described as "bounce off" leading to a finite v_1 and "squeeze out" leading to a finite v_2 [15]. Both v_1 and v_2 can be generated using models in their cascade mode as illustrated for the JAM model in Fig. 9, although the magnitudes do not accurately describe the data. In contrast, the observed $v_3\{\Psi_1\}$ cannot be generated by a cascade model as shown in Fig. 10. In the cascade mode, virtually no $v_3\{\Psi_1\}$ is developed in the models. As cascade models are incapable of generating $v_3\{\Psi_1\}$, the detection of $v_3\{\Psi_1\}$ necessitates an alternate driving force which can be provided by a nuclear potential as described in section V C.

Figs. 11(a-c) and Figs. 11(d-f) show comparisons of the data with JAM and SMASH simulations, respectively, where potentials have been included in the model. JAM $v_3\{\Psi_1\}$ and SMASH $v_3\{\Psi_1\}$ values are shown vs. rapidity, p_T, and centrality. For JAM and SMASH vs. centrality, we show values for π^+, π^- and protons. (The eccentricity, ϵ_3, will be discussed later.)

Note that centrality for the models uses cuts in the impact parameter b, where we assume that the nucleus is a spherical ball with radius 6.64 fm. The introduction of potentials reproduces the trends of the $v_3\{\Psi_1\}$ observed in the data as a function of rapidity, p_T, and centrality. Both models appear to have a weaker response

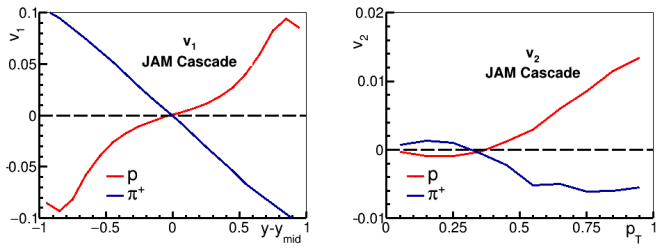

FIG. 9. (a) v_1 vs. rapidity for protons and π^+ in 3 GeV center of mass "minimum bias" Au+Au collisions as given by the JAM model in cascade mode. (b) v_2 vs. $p_{\rm T}$ for protons and π^+ in 3 GeV CM "minimum bias" Au+Au collisions as given by the JAM model in cascade mode.

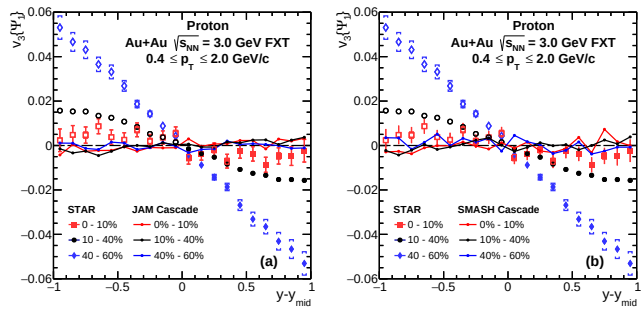

FIG. 10. $v_3\{\Psi_1\}$ for protons in several centralities in the JAM model (left) and SMASH model (right) as compared to the data. Cuts to the model are identical to the data, where centrality is defined by cuts in impact parameter as described in the text.

for peripheral collisions than the data, although JAM is slightly better; this is reflected in the rapidity and $p_{\rm T}$ distributions as well as the centrality distributions for peripheral events (Figs. 11(e-f)). JAM has a slightly weaker response, i.e. smaller $v_3\{\Psi_1\}$, than SMASH at higher $p_{\rm T}$ for mid-central collisions (compare Figs. 11(b) and 11(e)).

B. Role of Collision Geometry

The non-central collision of two large nuclei at low energies where stopping is strong, can result in a triangular geometry at rapidities away from $y_{\rm CM} = 0$. The stopping is a result of a combination of the nucleon-nucleon cross section, the collision energy which sets the time-scales, and the nuclear thickness. The origin of the triangular shape primarily stems from the uneven stopping by one nucleus onto the other in non-central events, with stronger stopping on one side for a specific rapidity region, as depicted in Fig. 12(a). The red triangle's lines in Fig. 12(b) portray the gradients leading to pressure in the red arrows' direction, yielding a negative $v_3\{\Psi_1\}$.

In order to study the relevant geometry in simulations where we can examine particles in configuration space, we select participant protons by requiring them to have a rapidity between $0.6 < y < 0.85$ and $0 < p_{\rm T} < 2$ GeV/c. We then use the models to plot the x and y positions of the protons in this region at $t = 50$ fm/c from the beginning of the simulation, when the flow has fully developed, but the triangular geometry is still visible although some expansion of the medium has already occurred. Figure 13 illustrates the spatial configuration of all such protons in 40-60% centrality collisions. We ensure the rapidity to be away from beam rapidity ($y = 1.05$) to select participants, although at low center-of-mass energy, the separation of participants and spectators is not as apparent as at higher energies, since there is time for the particles in the participant region to be scattered into the spectator region, and vice-versa. The half-moon shape, yielding the spacial distribution with a third harmonic (i.e. the triangular shape) necessary to seed $v_3\{\Psi_1\}$, is clearly visible.

To quantify the shape, we compute the third moment of the eccentricity ϵ_3 as a function of centrality. We make the assumption that it is odd in rapidity and keep the sign of the cosine term to allow for a negative value. Here, ϕ represents the angle between the particle and the reaction plane. The reaction plane angle is set to $\Psi_r = 0$ in both SMASH and JAM for all events. We then have

$$\epsilon_3 = -\frac{\langle r^2 cos(3(\phi - \Psi_r))\rangle}{\langle r^2\rangle}. \quad (4)$$

In these calculations, the origin was reset to the center of the distribution. Figs. 11(g-i) display the results for ϵ_3 using the JAM model at $t = 20$ fm/c, considering particles sorted by rapidity or $p_{\rm T}$. The time $t = 20$ fm/c was chosen to allow spectators to distinguish themselves from the participants; the flow had not yet fully developed.

The trends in ϵ_3 are clearly reflected in the data, indicating that the initial geometry, as quantified by the eccentricity, provides the necessary shape to seed the $v_3\{\Psi_1\}$ observed in the data. The observed flow is a function of both the shape and the potential which we discuss next.

C. Role of Mean Field Potentials

Mean field potentials have been used to describe collisions with nuclear targets at low energies. Several early models, successful in describing heavy-ion collisions, incorporated hadronic potentials [30–32]. Among the potentials were non-realtivistic Skyrme potentials and relativistic mean field potentials. The latter incorporated exchange particles such as the σ (scalar-isoscalar) and ω (vector-isoscalar) mesons. As center-of-mass energies increase, relativistic effects become more prominent. Some potentials allow for the sensitivity to phase transitions; however to accurately account for the transition to the Quark-Gluon Plasma, a transition to a hydrodynamic simulation is probably needed. As mentioned in the introduction, previous studies have shown that for

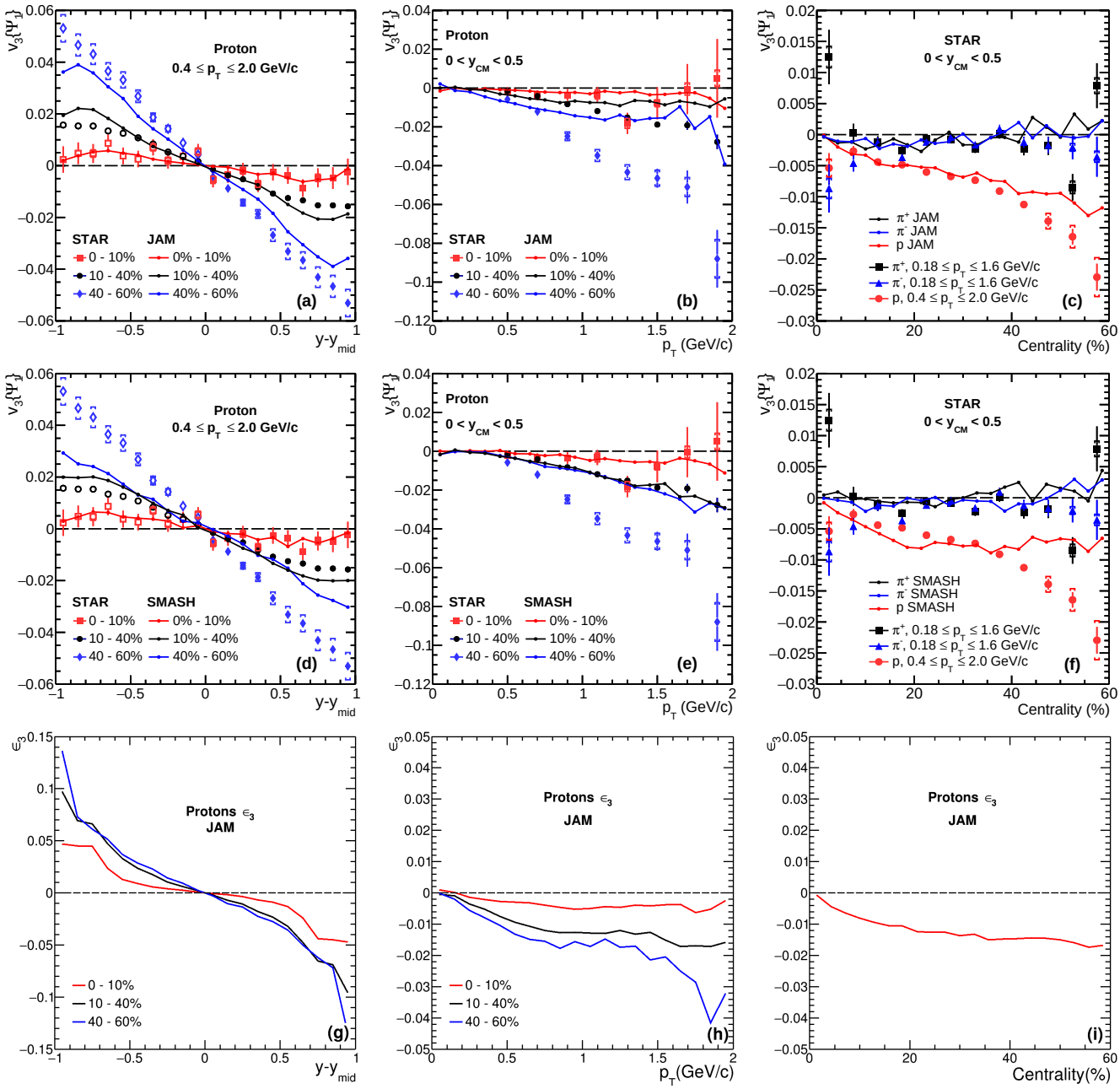

FIG. 11. The top two rows show fits of JAM (top row, Figs. (a-c)) and SMASH(2nd row, Figs. (d-f)) to the $v_3\{\Psi_1\}$ data vs. rapidity (first column), $p_{\rm T}$ (2nd column) and centrality (3rd column). The fits to distributions vs. rapidity and $p_{\rm T}$ (a,b,d,e) are fits to protons, for three centrality bins. Hollow points in Figs. (a,d) are reflected around the mid-rapidity as explained in the text. Fits to centrality (c,f) show protons, π^+, and π^-. The bottom row (Figs. (g-i)) depicts ϵ_3 in the JAM simulation for protons at $t = 20$ fm/c vs rapidity, $p_{\rm T}$ and centrality.

$\sqrt{s_{\rm NN}} \lesssim 4$ GeV mean field effects are important to explain observed directed and elliptic flow [15, 31, 33, 34]. This also holds true in our case.

To generate $v_3\{\Psi_1\}$, the introduction of a baryon density dependent potential was necessary. In the SMASH model, primarily aimed at low energy collisions below $\sqrt{s_{\rm NN}} = 3$ GeV, a Skyrme+Symmetry potential was used. Fermi motion and Pauli blocking were incorporated. The potential in SMASH is taken as

$$U = A(\rho/\rho_0) + B(\rho/\rho_0)^\tau \pm 2S_{\rm pot}\frac{\rho_{I_3}}{\rho_0} \qquad (5)$$

where ρ is the baryon density and ρ_{I_3} is the baryon isospin density of the relative isospin projection I_3/I. $\rho_0 = 0.1681/\text{fm}^3$ is the nuclear ground state density. Parameters for the Skyrme potential are $A = -124.0$ MeV, $B = 71$ MeV, and $\tau = 2$. For the Symmetry potential,

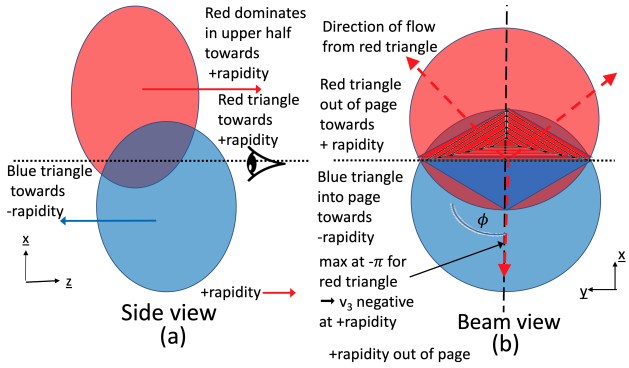

FIG. 12. Illustration of the triangular geometry of participants as discussed in the text. (a) Side view. The collision bifurcates the participants as indicated by the dotted line, where the nucleus from one half must penetrate through a thicker portion of the the other nucleus, thereby experiencing more stopping. (b) Beam view. The familiar almond shape formed by the participants resulting in v_2 primarily at mid-rapidity, is evident. However, at higher rapidity, the nucleons forming the half-moon shape with non-zero triangle component from the red nucleus penetrate through the thin tip of the blue nucleus, while the remainder of the nucleons from the red nucleus which participate in the collision, are stopped by the blue nucleus. The triangular shape emerges from the usual almond-shaped collision region, half of which is obstructed by the opposing nucleus. The lines in the red triangle portray the pressure gradients along the directions of the red arrows, resulting in a negative $v_3\{\Psi_1\}$.

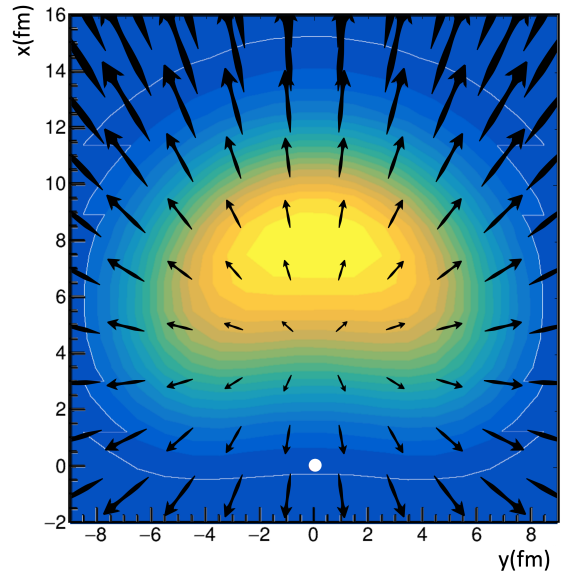

FIG. 13. Illustration of the x vs. y position of protons from JAM at $t = 50$ fm/c for particles with rapidity $0.6 < y < 0.85$ and $0 < p_{\rm T} < 2$ GeV/c (avoiding spectators) illustrating the half-moon, "triangular" shape. Note that the high density region is centered at x $\sim$ 7 fm. The arrows depict the vector field obtained by dividing the collision region into cells. The average momentum in each cell is superimposed on the original plot. The length of each arrow represents the magnitude of the average momentum in each cell. The white dot indicates the $x = 0$, $y = 0$ position.

$S_{pot} = 18$ MeV and the positive and negative signs refer to neutrons and protons, respectively. This model also reproduces an incompressibility of $K = 380$ MeV. These values are taken from values used by URQMD, which gave reasonable fits to preliminary HADES data on v_1, v_2 and $v_3\{\Psi_1\}$ [35].

We employed a relativistic mean field in the JAM1 model (RQMD.RMF)[3]. The potential invokes a relativistic mean field theory incorporating σ- and ω-meson-baryon interactions and momentum-dependent potentials as described in [37]. The parameter set MD2, described in the reference, has the same incompressibility as the SMASH model we used ($K = 380$ MeV). The parameter set yields results that are consistent with numerous data sets on sidewards flow $\langle p_x \rangle$ from mid-central Au+Au collisions from E895 and E877 at $\sqrt{s_{\rm NN}} = 2.7$–4.86 GeV. STAR and NA49 v_1 from mid-central Au+Au at $\sqrt{s_{\rm NN}} < 8.87$ GeV are also consistent with JAM using the MD2 parameter set. It is also consistent with the recent $\sqrt{s_{\rm NN}} = 3$ GeV proton directed and elliptic flow results [13]. However, above $\sqrt{s_{\rm NN}} = 8.87$ GeV, an additional attractive orbit is required, consistent with a softening of the equation of state (EOS). Figure 14 depicts the energy per nucleon vs. ρ/ρ_0 used in the two models in this work. Note that higher baryon density regions are to the right and the force will be towards lower baryon density regions. This will naturally produce a pressure away from regions of high baryon density, typically outwards in a collision.

To visualize the motion of the medium, the density plot shown in Fig. 13 is divided into cells and the average momentum is computed for each cell. The resulting vector field is superimposed on the original plot clearly showing the outward motion of the medium. Both the momentum vector and the density of the medium must be considered to obtain the flow. The white dot in the center indicates the origin in the x-y plane. The snapshot is taken at a time for $t = 50$ fm/c when the flow has had time to develop fully but the spacial configuration of the nucleons is still visible.

We now have identified the two essential ingredients required to generate $v_3\{\Psi_1\}$: (1) the initial condition supplied by the triangular shape resulting from a combination of the centrality and stopping, and (2) the force on the medium supplied by the potential.

[3] While the term RQMD is often used as the name of the code developed by Sorge, Stoecker and Greiner [36], the term RQMD is used for the underlying theoretical N-body model [14].

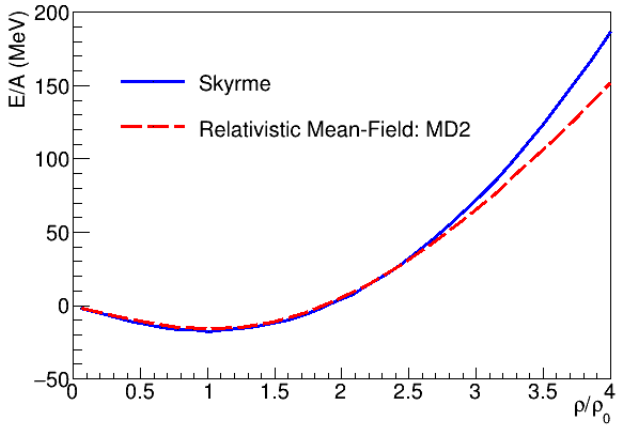

FIG. 14. Total energy per nucleon for the potential used in the models. The relatively hard Skyrme potential with $K = 380$ MeV used in the SMASH model is shown as the blue-solid line. The relativistic mean field potential with parameter set MD2 used in the JAM model is shown as the dashed red line [37]

.

D. Pions and Kaons

Figures 4 and 5 indicate that $v_3\{\Psi_1\}$ for π^+, π^-, and K^+ are essentially zero within $\sim 0.5\%$. $v_3\{\Psi_1\}$ for K^- may be negative, but that is at most a 1σ effect. The potentials used in the models only act on baryons. Any effect from these potentials on pions or kaons, such as on v_1, stem from secondary interactions resulting from the multiple scattering off baryons or from decays [17]. The models do not generate any $v_3\{\Psi_1\}$ for pions or kaons, hence $v_3\{\Psi_1\}$ appears to be a uniquely sensitive probe for a baryon density dependent mean-field potential. Since $v_3\{\Psi_1\}$ is only present for baryons in the data, it appears that the potential affects only baryons. Hence the presence of $v_3\{\Psi_1\}$ produced by a mean field potential acting only on baryons lends support to the conclusions of Ref. [13] that the collisions studied here are in the hadronic phase where protons and neutrons are the dominant degrees of freedom and not the partonic phase.

E. Comparison to HADES Results at $\sqrt{s_{\rm NN}} = 2.4$ GeV

In order to make a comparison with HADES results at $\sqrt{s_{\rm NN}} = 2.4$ GeV we employed the same selection of criteria for protons (20-30% centrality and $1.0 < p_{\rm T} < 1.5$ GeV/c) [11] and extracted slope measurements from both energies. Using these selection criteria we replicated the plot from Fig. 6 fitting it in the range $-0.5 < y_{\rm CM} < 0.5$ with the same equation as before - $y = ax + bx^3$. Our resulting slope measurement was $dv_3/dy = -0.053 \pm 0.004$. We then applied the same fit to the data published by HADES for the proton $v_3\{\Psi_1\}$ which yielded a slope measurement of $dv_3/dy = -0.243 \pm 0.010$. This is about a factor of five larger than the value we obtained at $\sqrt{s_{\rm NN}} = 3.0$ GeV.

This may imply that the effect of the mean field's influence is considerably stronger, even though the center-of-mass energy is lower by only 0.6 GeV. However, we must be cautious in that the center-of-mass energy may not be the relevant parameter. It is worth noting that, while the center-of-mass energy is only different by about 15%, the available kinetic energy is about a factor of two more at $\sqrt{s_{\rm NN}} = 3.0$ GeV. These observations prompt a need for further investigation into the physics that underlie these results to clarify and explain these disparities.

VI. SUMMARY

$v_3\{\Psi_1\}$ correlated with the reaction plane has been measured in Au+Au collisions at 3 GeV in the Beam Energy Scan II at RHIC. The effect is seen predominantly for baryons (protons). $v_3\{\Psi_1\}$ values show a negative slope as a function of $y_{\rm CM}$, opposite to that of v_1 at this energy. Its magnitude is larger at higher rapidity, increases as one goes to higher $p_{\rm T}$ and towards more peripheral collisions.

The development of $v_3\{\Psi_1\}$ is controlled by two key ingredients: the first is an appropriate geometry dictated by stopping, the passing time of the spectators, and the expansion of the fireball; the second is a potential in a responsive medium that drives the collective motion of particles. When compared with two theoretical models, JAM and SMASH, our data suggests that the required triangular geometry is a result of the dynamics of the collision, primarily from the nucleon-nucleon cross section, the energy, and the nuclear thickness which essentially bifurcates the nucleus when observed from one side in rapidity (stopping). In the models, JAM and SMASH, the force propelling the flow is provided by a potential which is a function of baryon density. Interestingly, it seems to affect only baryons and not mesons, at least within the statistical precision allowed by our present data set. In the models, any effects on mesons originate from the decays of excited baryons, or scattering, i.e. cascade type reactions. This, together with the fact that our data is consistent with these models, suggests that the medium is not in a partonic state and hence is below the QCD phase transition, consistent with the conclusions of previous STAR publications at $\sqrt{s_{\rm NN}} = 3$ GeV [13, 27].

A comparison with the HADES proton data indicates that the $v_3\{\Psi_1\}$ developed at $\sqrt{s_{\rm NN}} = 3$ GeV is much smaller than that at $\sqrt{s_{\rm NN}} = 2.4$ GeV. This does not necessarily mean that the mean field itself is stronger, in fact the parameters of the potential are probably similar as the energy increases, until a major change, such as a phase transition occurs. It is very likely that the geometry of the collision region is different at the two

energies, for instance because stopping is different; hence this would change the effect of the potential on the motion of the medium.

Future data sets at higher energies should yield more information on the potential and its efficacy, as these will modify both the medium, particularly when transitioning through the phase change, and the geometry due to the decrease in stopping. The $v_3\{\Psi_1\}$ studied here can be used as a particularly sensitive probe to examine the validity of a model in which a mean field is used to describe the data, since $v_3\{\Psi_1\}$ does not seem to be developed from a cascade model. Detailed comparisons can begin to determine the form of the potential, although certain aspects such as the definition of centrality in the models should be revised to be more reflective of the definitions used in the data. This was not done here to keep the comparison simple. Before multiplicity is used in the models to define centrality, a careful comparison of the particle multiplicities, rapidity, and p_{T} distributions must be performed.

An upcoming data sample with more than 5 times more statistics should yield more information, particularly for the K^-, and to verify whether the effect is exclusive to baryons, or whether there is a small effect for mesons. If the effect is only present for baryons, the disappearance of $v_3\{\Psi_1\}$ at higher energies may provide a signature for a situation in which baryons are no longer dominant and other degrees of freedom, e.g. constituent quarks, become important. In addition, the new data set will have increased PID capabilities as a new TOF detector (eTOF) which will extend time-of-flight coverage to η=1.5 (on the negative rapidity side using the coordinate system used in this analysis) was installed during data taking[38]. Finally, we will be able to study this effect over the entire energy range covered by BES II.

ACKNOWLEDGMENTS

We thank the RHIC Operations Group and RCF at BNL, the NERSC Center at LBNL, and the Open Science Grid consortium for providing resources and support. This work was supported in part by the Office of Nuclear Physics within the U.S. DOE Office of Science, the U.S. National Science Foundation, National Natural Science Foundation of China, Chinese Academy of Science, the Ministry of Science and Technology of China and the Chinese Ministry of Education, the Higher Education Sprout Project by Ministry of Education at NCKU, the National Research Foundation of Korea, Czech Science Foundation and Ministry of Education, Youth and Sports of the Czech Republic, Hungarian National Research, Development and Innovation Office, New National Excellency Programme of the Hungarian Ministry of Human Capacities, Department of Atomic Energy and Department of Science and Technology of the Government of India, the National Science Centre and WUT ID-UB of Poland, the Ministry of Science, Education and Sports of the Republic of Croatia, German Bundesministerium für Bildung, Wissenschaft, Forschung and Technologie (BMBF), Helmholtz Association, Ministry of Education, Culture, Sports, Science, and Technology (MEXT) and Japan Society for the Promotion of Science (JSPS).

[1] G. Odyniec (STAR), Beam Energy Scan Program at RHIC (BES I and BES II) – Probing QCD Phase Diagram with Heavy-Ion Collisions, PoS **CORFU2018**, 151 (2019).

[2] B. Müller, QCD Phase Boundary and the Hadrochemical Horizon, MDPI Physics **4**, 597 (2022), arXiv:2204.06998 [hep-ph].

[3] A. M. Poskanzer and S. A. Voloshin, Methods for analyzing anisotropic flow in relativistic nuclear collisions, Phys. Rev. C **58**, 1671 (1998), arXiv:nucl-ex/9805001.

[4] W. Reisdorf and H. G. Ritter, Collective flow in heavy-ion collisions, Ann. Rev. Nucl. Part. Sci. **47**, 663 (1997).

[5] C. Pinkenburg *et al.* (E895), Elliptic flow: Transition from out-of-plane to in-plane emission in Au + Au collisions, Phys. Rev. Lett. **83**, 1295 (1999), arXiv:nucl-ex/9903010.

[6] U. Heinz and R. Snellings, Collective flow and viscosity in relativistic heavy-ion collisions, Ann. Rev. Nucl. Part. Sci. **63**, 123 (2013), arXiv:1301.2826 [nucl-th].

[7] R. J. Fries, B. Muller, C. Nonaka, and S. A. Bass, Hadron production in heavy ion collisions: Fragmentation and recombination from a dense parton phase, Phys. Rev. C **68**, 044902 (2003), arXiv:nucl-th/0306027.

[8] J. C. Dunlop, M. A. Lisa, and P. Sorensen, Constituent quark scaling violation due to baryon number transport, Phys. Rev. C **84**, 044914 (2011), arXiv:1107.3078 [hep-ph].

[9] Z.-W. Lin, Extension of the Bjorken energy density formula of the initial state for relativistic heavy ion collisions, Phys. Rev. C **98**, 034908 (2018), arXiv:1704.08418 [nucl-th].

[10] L. Adamczyk *et al.* (STAR), Beam Energy Dependence of the Third Harmonic of Azimuthal Correlations in Au+Au Collisions at RHIC, Phys. Rev. Lett. **116**, 112302 (2016), arXiv:1601.01999 [nucl-ex].

[11] J. Adamczewski-Musch *et al.* (HADES), Directed, Elliptic, and Higher Order Flow Harmonics of Protons, Deuterons, and Tritons in Au + Au Collisions at $\sqrt{s_{NN}} = 2.4$ GeV, Phys. Rev. Lett. **125**, 262301 (2020), arXiv:2005.12217 [nucl-ex].

[12] B. Kardan (HADES), Collective flow measurements with HADES in Au+Au collisions at 1.23A GeV, PoS **CPOD2017**, 049 (2018).

[13] M. S. Abdallah *et al.* (STAR), Disappearance of partonic collectivity in $\sqrt{s_{NN}} = 3$ GeV Au+Au collisions at RHIC, Phys. Lett. B **827**, 137003 (2022), arXiv:2108.00908 [nucl-ex].

[14] Y. Nara and H. Stoecker, Sensitivity of the excitation functions of collective flow to relativistic scalar and vector meson interactions in the relativistic quantum molecular

dynamics model RQMD.RMF, Phys. Rev. C **100**, 054902 (2019), arXiv:1906.03537 [nucl-th].

[15] S. A. Bass *et al.*, Microscopic models for ultrarelativistic heavy ion collisions, Prog. Part. Nucl. Phys. **41**, 255 (1998), arXiv:nucl-th/9803035.

[16] J. Weil *et al.* (SMASH), Particle production and equilibrium properties within a new hadron transport approach for heavy-ion collisions, Phys. Rev. C **94**, 054905 (2016), arXiv:1606.06642 [nucl-th].

[17] A. Sorensen, Private communication (2023).

[18] K. H. Ackermann *et al.* (STAR), STAR detector overview, Nucl. Instrum. Meth. A **499**, 624 (2003).

[19] M. Anderson *et al.*, The Star time projection chamber: A Unique tool for studying high multiplicity events at RHIC, Nucl. Instrum. Meth. A **499**, 659 (2003), arXiv:nucl-ex/0301015.

[20] W. J. Llope *et al.*, The TOFp / pVPD time-of-flight system for STAR, Nucl. Instrum. Meth. A **522**, 252 (2004), arXiv:nucl-ex/0308022.

[21] J. Adams, A. Ewigleben, S. Garrett, W. He, T. Huang, P. Jacobs, X. Ju, M. Lisa, M. Lomnitz, R. Pak, R. Reed, A. Schmah, P. Shanmuganathan, M. Shao, X. Sun, I. Upsal, G. Visser, and J. Zhang, The star event plane detector, Nucl. Instrum. Meth. A **968**, 163970 (2020).

[22] M. S. Abdallah *et al.* (STAR), Global Λ-hyperon polarization in Au+Au collisions at $\sqrt{s_{NN}}$=3 GeV, Phys. Rev. C **104**, L061901 (2021), arXiv:2108.00044 [nucl-ex].

[23] M. S. Abdallah *et al.* (STAR), Measurements of Proton High Order Cumulants in $\sqrt{s_{\rm NN}} = 3$ GeV Au+Au Collisions and Implications for the QCD Critical Point, Phys. Rev. Lett. **128**, 202303 (2022), arXiv:2112.00240 [nucl-ex].

[24] H. Masui, A. Schmah, and A. M. Poskanzer, Event plane resolution correction for azimuthal anisotropy in wide centrality bins, Nucl. Instrum. Meth. A **833**, 181 (2016), arXiv:1212.3650 [physics.data-an].

[25] See Supplemental Material at [URL will be inserted by publisher] for a comparison of R_{31} and R_{11}.

[26] R. Barlow, Systematic errors: Facts and fictions, in *Conference on Advanced Statistical Techniques in Particle Physics* (2002) pp. 134–144, arXiv:hep-ex/0207026.

[27] M. S. Abdallah *et al.* (STAR), Light nuclei collectivity from $\sqrt{s_{NN}} = 3$ GeV Au+Au collisions at RHIC, Phys. Lett. B **827**, 136941 (2022), arXiv:2112.04066 [nucl-ex].

[28] Z.-W. Lin, C. M. Ko, B.-A. Li, B. Zhang, and S. Pal, Multiphase transport model for relativistic heavy ion collisions, Phys. Rev. C **72**, 064901 (2005).

[29] B. B. Back, R. R. Betts, J. Chang, W. C. Chang, C. Y. Chi, Y. Y. Chu, *et al.* (E917), Baryon rapidity loss in relativistic Au+Au collisions, Phys. Rev. Lett. **86**, 1970 (2001), arXiv:nucl-ex/0003007.

[30] B. D. Serot and J. D. Walecka, Recent progress in quantum hadrodynamics, Int. J. Mod. Phys. E **6**, 515 (1997), arXiv:nucl-th/9701058.

[31] O. Buss, T. Gaitanos, K. Gallmeister, H. van Hees, M. Kaskulov, O. Lalakulich, A. B. Larionov, T. Leitner, J. Weil, and U. Mosel, Transport-theoretical Description of Nuclear Reactions, Phys. Rept. **512**, 1 (2012), arXiv:1106.1344 [hep-ph].

[32] B. Blaettel, V. Koch, and U. Mosel, Transport theoretical analysis of relativistic heavy ion collisions, Rept. Prog. Phys. **56**, 1 (1993).

[33] M. Bleicher *et al.*, Relativistic hadron hadron collisions in the ultrarelativistic quantum molecular dynamics model, J. Phys. G **25**, 1859 (1999), arXiv:hep-ph/9909407.

[34] A. Andronic *et al.* (FOPI), Excitation function of elliptic flow in Au+Au collisions and the nuclear matter equation of state, Phys. Lett. B **612**, 173 (2005), arXiv:nucl-ex/0411024.

[35] P. Hillmann, J. Steinheimer, and M. Bleicher, Directed, elliptic and triangular flow of protons in Au+Au reactions at 1.23 A GeV: a theoretical analysis of the recent HADES data, J. Phys. G **45**, 085101 (2018), arXiv:1802.01951 [nucl-th].

[36] A. von Keitz, H. Sorge, H. Stöcker, and W. Greiner, Microscopic models for ultra-relativistic collisions with massive nuclei, Nuclear Physics A **527**, 601 (1991).

[37] Y. Nara, T. Maruyama, and H. Stoecker, Momentum-dependent potential and collective flows within the relativistic quantum molecular dynamics approach based on relativistic mean-field theory, Phys. Rev. C **102**, 024913 (2020), arXiv:2004.05550 [nucl-th].

[38] The STAR Collaboration and The CBM Collaboration eTOF Group, Physics program for the star/cbm etof upgrade (2016), arXiv:1609.05102 [nucl-ex].

Reaction plane correlated triangular flow in Au+Au collisions at $\sqrt{s_{NN}} = 3$ GeV

The STAR Collaboration
(STAR Collaboration)
(Dated: September 13, 2023)

arXiv:2309.12610v1 [nucl-ex] 22 Sep 2023

I. EVENT PLANE RESOLUTION

As a sanity check that our event plane resolutions for triangular flow using the first-order event plane ($v_3\{\Psi_1\}$) are reasonable, the event plane resolutions for directed flow ($v_1\{\Psi_1\}$) were also calculated. Figure 1 shows a comparison between the event plane resolutions for $v_1\{\Psi_1\}$ and $v_3\{\Psi_1\}$, where both sets were calculated with this analysis. The systematic uncertainties for both sets were calculated the same way as described in the main text. It was found that the first order resolutions are consistent with Ref. [1].

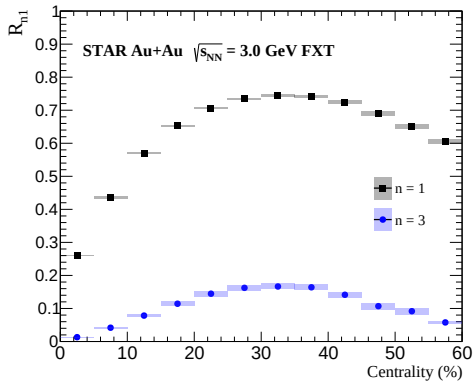

FIG. 1. Event plane resolution for $v_1\{\Psi_1\}$ and $v_3\{\Psi_1\}$ as a function of centrality from $\sqrt{s_{NN}} = 3$ GeV Au+Au collisions at STAR. The points are the average of the resolutions from the three configurations discussed in the main text, and the systematic uncertainties are the maximum difference between the configurations and the average (taken as a symmetric uncertainty in the opposite direction as well). Vertical lines are statistical uncertainties and shaded boxes are systematic uncertainties.

[1] M. S. Abdallah *et al.* (STAR), Disappearance of partonic collectivity in $\sqrt{s_{NN}} = 3$ GeV Au+Au collisions at RHIC, Phys. Lett. B **827**, 137003 (2022), arXiv:2108.00908 [nucl-ex].